Additive Manufacturing 126 (2026) 105262

Contents lists available at ScienceDirect

Additive Manufacturing

journal homepage: www.elsevier.com/locate/addma

Fibroprinting - hybrid fiber-reinforced (Bio)fabrication via in-situ biomimetic spinning and 3D printing

Waseem Kitana [a], Pavel Milkin [a], Ilia Sadilov [a], Olga Rusu [a], Md Fakrul Bin Kabir [a], Ceyda Topal [a], Selma Padilla Padilla [a], Janina Rebhan [a], Indra Apsite [a], Gissela Constante [a], Zhander Vohr Soreño [a], Alla Synytska [b,c,d,e], Leonid Ionov [a,b,d,e,*]

[a] Faculty of Engineering Science, University of Bayreuth, Ludwig-Thoma-Straße 36A, Bayreuth 95447, Germany
[b] University of Bayreuth, Universitätsstraße 30, Bayreuth 95447, Germany
[c] Functional Polymer Interfaces Research Group, Faculty of Engineering Science, University of Bayreuth, Ludwig-Thoma-Straße 36A, Bayreuth 95447, Germany
[d] biovature GmbH Bayreuth, Germany
[e] Bavarian Polymer Institute (BPI), Germany

ARTICLE INFO

Keywords:
3D printing
Fiber spinning
Fiber-reinforced
Biomaterials
Extrusion 3D print

ABSTRACT

One major challenge in the additive manufacturing of soft materials such as thermoplastics, elastomers, and gels is their low mechanical stability. Nature solves this by embedding continuous fibers like collagen or cellulose into soft matrices. Integrating 3D printing into composite materials with fiber spinning has remained difficult due to limited material compatibility, restricted deposition methods, insufficient control over fiber properties, and lack of interlayer reinforcement. We present a spider-inspired technology that combines 3D (bio) printing with *in situ* biomimetic fiber spinning allowing novel approach for additive manufacturing of fiber-reinforced composites. Fibers with diameter ranging from ca. 200 nm to ca. 20 μm of microns are drawn from polymer solutions or melts with maximal average speed up to ca. 4.4 m/s and deposited via controlled oscillatory motion with placement precision ca. 100 μm over distance of at least 10 cm, enabling horizontal or tilted freestanding fibers, precise adjustment of pulling speeds, and fabrication of structures with virtually unlimited thickness. This method surpasses many existing fiber-reinforced additive manufacturing techniques and enables novel complex, fiber-reinforced architectures and composites for biomedical and engineering applications by combining (i) fast deposition of very thin fibers; (ii) their programmed deposition and distribution; (iii) fabrication of free-standing fibers; and (iv) fabrication of samples with virtually unlimited thickness.

1. Introduction

Additive manufacturing (AM) or 3D printing techniques offer numerous advantages, including rapid prototyping, customized production, and design flexibility, allowing fabrication of structures with complex shapes. However, conventional polymer-based AM technologies [1] deliver only moderate mechanical performance. This is due to the reliance on polymers with moderate molecular weight that is needed to allow proper flow of polymer melt. High-performance polymers typically exhibit viscosities that are too high for conventional 3D printing processes or are processed in harsh conditions. Consequently, many applications remain limited to prototyping rather than functional, load-bearing components.

One approach to enhance the mechanical properties of 3D-printed parts is to use materials with strong bonds, such as metals or ceramics. This is one reason why sintering-based 3D printing methods are among the most commercially successful [2]. Weaker materials, such as polymers (thermoplastics, elastomers, and gels), can be mechanically reinforced by incorporating fibers to form fiber-reinforced composites. [3,4]. The fibers do not only make material stiffer that can be achieved by adding of particles but allow redistribute locally applied stress on large area improving crack resistance. In fiber form, polymer chains are uniaxially aligned, resulting in significantly higher elastic modulus and strength compared to their fiber-free counterparts. A common reinforcement strategy involves incorporating short fiber fragments into the polymer matrix. While this can modestly improve the material's strength, the presence of short fibers degrades flowability by introducing a threshold stress that hinders polymer flow and reduces interlayer

* Corresponding author at: Faculty of Engineering Science, University of Bayreuth, Ludwig-Thoma-Straße 36A, Bayreuth 95447, Germany.
E-mail address: leonid.ionov@uni-bayreuth.de (L. Ionov).

https://doi.org/10.1016/j.addma.2026.105262
Received 10 March 2026; Received in revised form 19 May 2026; Accepted 4 June 2026
Available online 5 June 2026
2214-8604/© 2026 The Author(s). Published by Elsevier B.V. This is an open access article under the CC BY license (http://creativecommons.org/licenses/by/4.0/).

adhesion.

Using long continuous fibers provides significantly greater reinforcement than short fibers. However, integrating continuous fibers into 3D printing processes presents considerable technical challenges. Co-extrusion with polymer filaments is one viable approach [5–7], but it is relatively slow and imposes limitations on the geometry and types of structures that can be fabricated. Moreover, this method is compatible with only a limited number of 3D printing techniques. Typically, the fibers are deposited along the filament path but not between layers, leaving interlayer adhesion as a persistent weakness.

Alternative strategies combine laboratory-scale fiber-spinning with 3D (bio) printing, but limitations in speed, precision, and scalability persist. Electrospinning [8] can generate micro- and nanofibers at high speeds, yet deposition control is poor, typically yielding disordered mats. Alignment methods—such as rotating drums or parallel electrodes—improve orientation but lack spatial accuracy and are difficult to integrate with 3D (bio) printing. Melt electrowriting [9] offers precise placement using relatively high-viscosity polymers at relatively low flow rates, but the process is slow (~50 $mm{\cdot}s^{-1}$). Stability requires drawing speeds below the polymer's inverse relaxation time, preventing deposition of long freestanding fibers with oriented polymer chains [10]. Consequently, neither electrospinning nor melt electrowriting can (i) produce long free-standing fibers capable of spanning large distances without sagging, and (ii) are limited to the fabrication of thin (millimeter-scale) samples, which altogether substantially restricts the capabilities of these methods.

Mechanical force-based spinning methods enable high stretching forces, which are crucial for chain alignment and improved mechanical properties [11]. Centrifugal and blow spinning approaches (pull spinning [12], centrifugal spinning, blow spinning [9,13]) offer high production rates but poor deposition precision and accuracy. Gravity-assisted methods [14,15] provide better placement control but require vertical setups and additional fiber collection machinery. Other techniques rely on stretching a polymer between two separating elements, e.g., two blocks (one with deposited solution), counter-rotating belts, or rods on rotating disks [16]. These approaches face challenges in achieving high acceleration or stretching speeds. Integrating such methods with 3D printing remains difficult due to limited deposition control, low spinning rates [17], or restrictive geometries [18–20]. Thus, integrating state-of-the-art fiber spinning with 3D printing remains highly challenging due to significant limitations.

2. Materials and methods

2.1. Materials

Poly[(R)−3-hydroxybutyric acid] (P3HB; average M_w ~ 400–500 kDa), polycaprolactone (average M_n ~ 45 and 80 kDa), poly (ethylene oxide) (PEO; average M_v ~ 100, 200, 600, 2000, 4000, 8000 kDa), poly(dimethylsiloxane) (PDMS), and hydroxy-terminated with kinematic viscosity 65 cSt were purchased from Merck KGaA (Darmstadt, Germany). Soft two component Silicon Dragon skin™ Slow 10, (Poly(ethylene oxide) (PEO, M_w ~ 1000 kDa) was obtained from Polysciences (PA, USA). Polycaprolactone (PCL 100 Filament) Facilan™ (M_w ~ 50 kDa) was purchased from 3D4Makers B.V (Haarlem, The Netherlands). Premium polylactic acid (PLA) filament C.C.Transparent was purchased from FormFutura B.V. (Amsterdam, The Netherlands). Polyhydroxalkonate (PHA) filament (allPHA) was obtained from colorFabb B.V. (Belfeld, The Netherlands). Nonoilen® filament made of polylactic acid and polyhydroxy butyrate blend (PLA/PHB) was purchased from Fillamentum Manufacturing (Hulín, Czech Republic). Nylon PA12 filament from Fiberlab S.A. (Brzezie, Poland). TPU Filament Filaflex 70 A from Recreus Industries S.L. (Alicante, Spain). Filaflex 88 A TPU Flex Semisoft from Extrudr - FD3D GmbH (Lustenau, Austria). Poly (1,4-butylene)-based poly (ester urethane) (PEU-PBA) and poly (1,10-decylene adipate)-based poly (ester urethane) (PEU-PDA) were obtained from Fraunhofer Institute for Applied Polymer Research IAP (Potsdam, Germany). Borax anhydrous, boric acid (H_3BO_3) (≥99.5%), and sodium carboxymethyl cellulose (SCMC) (average M_w 700 ~ kDa) were obtained from Merck KGaA (Darmstadt, Germany). Silicic acid lithium magnesium sodium salt (Laponite RD) was provided by BYK-Chemie GmbH (Wesel, Germany). Alginic acid sodium salt (M ~ 300–350 kDa) was purchased from Carl Roth GmbH + Co. KG (Karlsruhe, Germany).

Ethanol absolute (ACS reagent, ≥99.5%), Chloroform (ACS reagent, ≥99.8%), Toluene (ACS reagent, ≥99.5%) were obtained from Merck KGaA (Darmstadt, Germany). Tetrahydrofuran (Roth, ≥99.5%) was purchased from Carl Roth GmbH + Co. KG (Karlsruhe, Germany). Hexafluoroisopropanol (HFIP) (99%) was purchased from abcr GmbH (Karlsruhe, Germany).

For the cell culture experiments, the cell line BALB/3T3 fibroblasts clone A31-CCL−163 was purchased from American Type Culture Collection (ATCC) (Manassas, VA, USA) and used up to passage 7. Human Induced Pluripotent Stem Cell (hiPSC) SCTi003-A cell line (Female) with passage 32 and was purchased from STEMCELL technology (Vancouver, Canada). NHDF-Ad - Human Dermal Fibroblasts, Adult was obtained from Lonza Bioscience (Basel, Switzerland) and was used up to passage 6. Human Recombinant TGF-beta 1, mTeSR Plus, ReLeSR, STEMdiff Cardiomyocyte Differentation kit and STEMdiff Cardio Maintenance Kit were purchased from STEMCELL technology (Vancouver, Canada). SiR-actin kit was obtained from Spirochrome AG (Stein am Rhein, Switzerland). The 4′,6-diamidino−2-phenylindole (DAPI *BioChemica*) was purchased from AppliChem GmbH (Darmstadt, Germany). Formaldehyde solution 37% and Bovine Serum Albumin (BSA) (Fraction V) were purchased from Carl Roth GmbH + Co. KG (Karlsruhe, Germany). Phalloidin DyLight 488 conjugated 300 (300 $units{\cdot}mL^{-1}$) was purchased from Cell Signaling Technology Europe, The Netherlands. Dulbecco's Modified Eagle Medium (DMEM) (with 4.5 $g{\cdot}L^{-1}$ glucose, without L-glutamine and sodium pyruvate with 3.7 $g{\cdot}L^{-1}$ $NaHCO_3$) was purchased from PAN-Biotech GmbH (Aidenbach, Germany). Fetal Bovine Serum (FBS), GlutaMax Supplement 100X, Penicillin-Streptomycin 100X (5000 $U{\cdot}mL^{-1}$), Vybrant™ DiO Cell-Labeling Solution, and Collagen I Monoclonal Antibody (COL−1) were purchased from Thermo Fisher Scientific Inc. (Waltham, MA, USA). Goat Anti-Mouse IgG H&L (Alexa Fluor® 594) was obtained from Abcam Limited (Cambridge, UK). Cyanobacteria strain *Lyngbya lagerheimii* SAG 24.99 was purchased from University of Goettingen (Göttingen, Germany), Cyanobacteria BG−11 Freshwater solution, Dulbecco's Phosphate Buffered Saline (DPBS), Gentamicin solution (10 $g{\cdot}L^{-1}$ in deionized water, BioReagent), Triton X−100 (for molecular biology) were obtained from Merck KGaA (Darmstadt, Germany).

2.2. Solution's preparations

The PEO solutions were prepared by dissolving in MilliQ water ($\Omega{>}18.2M\Omega{\cdot}cm^{-1}$) and stirring at 100 rpm for around 3 days. The P3HB solutions (46–95 $g{\cdot}L^{-1}$) were prepared by dissolving in chloroform and stirring at 200 rpm in a 60 °C water bath for 3 h. PCL 80 kDa (150 $g{\cdot}L^{-1}$) blended with PEO 8000 kDa (7 $g{\cdot}L^{-1}$) was prepared by mixing the solutes in dry state and dissolving in chloroform for overnight at 150 rpm. The Nylon 6,6 solution was prepared by dissolving the polymer in HFIP and stirring at 200 rpm in a 45 °C water bath for 2 h.

Alginate-borax biomaterial ink solution was prepared as follows. Borax anhydrous stock solution was prepared in BALB/3T3 cell growth medium at a concentration of 20 mM. Next, alginate solution at a final concentration of 40 $g{\cdot}L^{-1}$ was prepared by adding borax solution to alginate powder and immediately manually stirred with a sterile spatula until homogeneous solution was achieved. The solution was left to stir at 150 rpm at room temperature for 12 h.

The alginate-SCMC biomaterial ink was prepared as described previously [21]. Shortly, alginate and SCMC powders were mixed in their dry state in two different ratios of 1.17:1 or 3.5:1. alginate-SCMC mix

was dissolved in water until reaching a final concentration of alginate in the solution of 35 g·L^{-1} and 30 g·L^{-1} of SCMC (ratio 1.17:1), or 10 g·L^{-1} of SCMC (ratio 3.5:1). The solution was kept stirring overnight at room temperature.

The alginate biomaterial ink was prepared by dissolving alginate in DMEM at a concentration of 35 and 40 g·L^{-1}.

The laponite gel was prepared as described previously [21]. The laponite-RD solution was prepared in water at a concentration of 50 g·L^{-1}. First, in a glass vial, the water was kept stirring at high rotational speeds of around 1000 rpm to form a vortex, and then laponite-RD powder was added gradually under constant stirring to avoid sudden gelation. The solution kept stirring at 1000 rpm for 20 min until a homogeneous, transparent dispersion was observed.

To prepare polyborosiloxane ($\lambda \sim 0.6$ s and plateau shear modulus (G) $\sim 10^4$ Pa), the mass ratio between the hydroxyl-terminated PDMS 65 cSt and H_3BO_3 100:0.88 was chosen. First, the PDMS was dissolved in toluene. Then, H_3BO_3 was added to the solution, and the mixture was dispersed for a couple of minutes in an ultrasonic bath. The mixture was heated to 120 °C with a Dean-Stark trap and left for 48 h with further stirring. After this time, the mixture became transparent. Excess solvent was removed with a vacuum evaporator, and the rest of the solvent was removed by storing the sample in a vacuum oven at 60 °C for 24 h.

2.3. Rheological characterization

A modular rheometer Anton Paar MCR 702 MultiDrive Rheometer (Anton Paar GmbH - Graz, Austria) was used to study the rheological characteristics of the polymer solutions and melts. PEO solutions and melts polymers (3D printing filaments). A frequency sweep was made in a range from 0.0628 to 628 rad·s^{-1} for all PEO solutions. Viscosity curves were performed in a range of 0.01–100 s^{-1}. In the case of the melts, the temperature was stabilized within 5 min. Three melting temperatures were chosen for every polymer to achieve the temperature dependence of zero-shear viscosity and characteristic time.

2.4. Scanning electron microscopy (SEM)

The SEM images of PEO fibers were made by using a scanning electron microscope Thermo Fischer Scientific Apreo 2 SEM (Waltham, USA). The sample was sputtered with 4 nm platinum to avoid charging effects. The information about the fiber diameters was achieved by using ImageJ software.

2.5. Sample's preparation

Samples were prepared by sequential 3D (bio) printing and mechanical fiber pulling (oscillation fiber spinning) using Fibrotiss© machine (developed by biovature GmbH – Bayreuth, Germany). The conditions for fiber spinning are given in the main text.

2.6. 3D printing of gels

The 3D printing conditions of biomaterial inks is as follows: The alginate-SCMC ink was 3D printed at a pneumatic pressure of 0.35 bar, extruded through a PTFE red tapered nozzle with an inner diameter of 250 μm (25 G), and a printing speed of 150 mm·min^{-1}. The infill distance was set to 1 mm, and the height between layers was set at 0.2 mm. The laponite solution was printed at 0.15 bar of pneumatic pressure with a nozzle (inner diameter 250 μm), and a printing speed of 200 mm·min^{-1}. The alginate-borax gel was printed at a speed of 40 mm·min^{-1} with an inner diameter 630 μm (20 G) PTFE pink tapered nozzle and pneumatic pressure of 4.5 bars. In addition to that, the layers were printed in an alternating pattern ("woodpile"-like structure), zigzag, concentric, or rectilinear. The alginate solution in DMEM media was printed by applying a constant pressure of 0.4 bar through a nozzle 250 μm (25 G) at a movement rate of 100 mm·min^{-1}.

2.7. 3D printing of melts

The spun fibers fixation frame was melt 3D printed using PLA filament in two different shapes; circle and square. For that an extrusion temperature of 190 °C, 50 mm·min^{-1}, concentric infill (2 concentric lines), and layer height of 0.3 mm. The first layer of PLA was 3D printed followed by oscillation spinning of P3HB fibers and finished by another layer of PLA melt 3D printing to fix the fibers in place.

2.8. Melt electrowriting

For the fiber-reinforced alginate, PCL 100 filament was melt electrowritten at 165°C using voltage of 3 kV. The distance between the platform and extruder was 3 mm, and the printing speed was 400 mm·min^{-1}.

2.9. Filament fabrication

PCL 45 kDa and 80 kDa filaments were prepared using a custom-made filament extruder. The polymer melted at 50 °C for 45 kDa and 100 °C for 80 kDa before extrusion. The filament was extruded through a metallic nozzle with an inner diameter of 1.75 mm at a constant extrusion rate of 10 mm min^{-1}.The molten filament was rapidly cooled with a ventilator while being pulled.

2.10. Melt spinning of polymers

Through filament-fused extrusion, the polymer was spun by oscillatory spinning at temperatures over the melting point at lower opm. Table S1 and Figure S11 present the temperature of spinning and observations from the melt spinning of filaments.

2.11. Fiber-reinforced silicone composite

For the fiber-reinforced Dragon Skin™ soft silicon the Nylon 6,6 fibers were spun on top of the 3D printed support cream-like structure in layer-by layer manner (5 layers of support and 4 layers of fibers). The obtained structure was filled with premixed and degassed mixture of Dragon Skin™ silicone followed by placing the sample in vacuum for faster filling of interfiber space and left for 24 h to cure. The reference sample without fibers was cured in the same manner in a 3D printed mold.

2.12. Electrospinning

PEO solutions were electrospun by a custom-made device. Nozzle diameter was 800 μm (G21), distance between nozzle and collector was 11.5 cm, and applied voltage was 15 kV. Applied pressure to the solution was between 0.01 mL·min^{-1} and 0.025 mL·min^{-1}.

2.13. Tensile testing

The modular rheometer (Anton Paar MCR 702 MultiDrive Rheometer, Anton Paar GmbH, Graz, Austria) was used to study tensile properties of the fiber alone and fibers combined non-crosslinked alginate gel in uniaxial mode and immersed in PBS at 37°C. The fiber alone sample was tested at 0.1%·s^{-1} strain rate. Strain-stress measurements were performed for P3HB fibers and alginate gel sandwich structure. Final strain was 10% with a strain rate 0.5%·s^{-1}.

2.14. Actin filament (F-actin) – cell nucleus staining

BALB/3T3 fibroblasts at a cell density of 1 million cells·mL^{-1} were seeded on the different P3HB fibrous structures to study the organization of fibroblasts by visualizing the actin filaments of the cell body and cell nucleus at day 6 of incubation. The final staining solution was composed

of 1:400 dilution of Phalloidin Dylight 488, and 0.1 μg·mL^{-1} DAPI (5 g·L^{-1} in dimethylformamide) in PBS. Firstly, the medium was removed from the samples, and the samples were washed three times with PBS for 5 min each. Next, the cells were fixed with 3.7% (*v/v*) formaldehyde in PBS for 15 min and washed three times with PBS. After that, the permeabilization solution (Triton 100 X solution in PBS at a concentration of 1 μg·mL^{-1}) was added to the samples and incubated for 5 min at room temperature, and then washed three times with PBS. Finally, the Phalloidin and DAPI-containing staining solution was added to the samples and incubated for 30 min at room temperature. Following that, the staining solution was aspirated and washed three times with PBS. At the end, the samples were kept in PBS and visualized under the Nikon Ti2 fluorescence microscope (Nikon Eclipse Ti2 inverted microscope, Nikon Instruments Inc., Japan).

2.15. Collagen type I immunostaining

Normal human dermal fibroblasts (NHDF) at a cell density of 1.1 million cells·cm^{-2} were seeded on the P3HB fibrous samples (bundled fibers). To stimulate ECM proteins deposition, such as collagen type I, transforming growth factor beta 1 (TGF-β) was added to the samples. In addition to that, a sample without TGF-β was used as a control. The TGF-β working solution was prepared at a final concentration of 3 ng·mL^{-1} in growth media. After 7 days of incubation, the samples were stained to visualize collagen type I and F-actin. For that, the samples were first washed once with PBS for 5 min, followed by fixing the samples with 3.7% *(v/v)* formaldehyde solution in PBS for 30 min at room temperature. Next, the cell fixation solution was removed from the samples, followed by cell permeabilization using a mixture of 0.1% *(v/v)* Triton X−100 and 1 g·L^{-1} BSA in PBS 3x with a duration of 5 min each. In the next step, a blocking solution of 30 g·L^{-1} BSA in PBS was added for 30 min at room temperature. After removing the blocking solution, the samples were washed with 0.1% Triton X−100 – 1 g·L^{-1} BSA solution for 3 times, 5 min each. Following that, the blocking solution was pipetted out from the samples and the primary antibody collagen I Monoclonal Antibody (COL−1) produced in mouse (1:100 dilution) in the 0.1% Triton X−100 – 1 g·L^{-1} BSA solution were incubated for overnight at 4 °C. Next, the samples were washed with 0.1% Triton X−100 in PBS for 3 times, and then the secondary antibody goat anti-mouse IgG H&L (Alexa Fluor® 594) (ab150116) (1:400 dilution) in 0.1% Triton X−100–1 g·L^{-1} BSA in PBS solution was added to the samples and incubated for 3 h at room temperature. Next, the secondary antibody solution is aspirated, and the samples are washed with PBS three times, 5 min each. Finally, DAPI and Phalloidin at a concentration of 0.1 μg·mL^{-1} and 1:400 dilution in PBS were added to counterstain the cell nuclei and F-actin, respectively. Next, the samples were incubated at room temperature for 30 min.

2.16. Live cell microscopy

NHDF cells (0.4 million cells·cm^{-2}) motility was visualized on the oscillation spun P3HB aligned fibers using the ND acquisition mode (time control) of the NIS-Elements software of the Nikon Ti2 fluorescence microscope. For this, NHDF cells were stained in suspension with Vybrant™ DiO cell-labeling solution according to the manufacturer's instructions and incubated initially for 30 min before visualizing under the microscope. After incubation for 30 min, the sample was then installed in the stage top incubator chamber with air, CO_2, humidity, and temperature controllers (UNO stage top incubator, H301-NIKON-TI-S-ER xy-motorized stage with 2GF-mixer, OKOLAB S.R.L., Italy). The temperature of the incubator was set to 37°C with air and CO_2 flow controlled to get 95% air and 5% CO_2, as well as a humidity level of greater than 85%. Time-lapse image sequence of the fibroblasts was acquired with a total duration of 24 h at 20x magnification two days after incubation (1 frame every 15 min – total 97 frames). The generated time-lapse sequence was acquired in bright field and FITC channels with 5 Z-stack loops of a step size of 8.3 μm. The exported video was saved with a 15 s (97 frames x 150 ms) duration (2D) and 70 s (97 frames x 700 ms) duration (3D). The 3D video was deconvoluted with 100 iterations using the Richardson-Lucy deconvolution method.

2.17. 3D bioprinting of cardiomyocytes

Cardiomyocytes were differentiated from hiPSCs following the manufacturer's (STEMCELL technology) differentiation protocol. Differentiated beating cardiomyocytes were harvested using ReLeSR cell detachment solution. Cell density of 30 million cells·mL^{-1} was used for bioink preparation. Cardiomyocytes were mixed in the gels alginate-SCMC (preparation described above) to reach the required cell density in bioink. Sample preparation and bioprinting were done with a moving profile as described above, in total repeating three repeats of fiber and bioink layers. To track viable cells in the 3D construct SirActin at a concentration of 1 μM was added to the bioink and vortexed briefly to ensure cell tracking after printing. Images were taken 5 h after printing to observe cell viability and the capability to move to fibers.

2.18. Spinning of cyanobacteria

A solution of 40 g·L^{-1} of PEO 2000 kDa in deionized water was prepared by constant stirring overnight at room temperature. An aggregate of cyanobacteria was collected from the liquid media and ground with metallic balls to produce uniform dispersion. This step ensures proper spinning and avoids clogging of the nozzle. The PEO solution and cyanobacteria were mixed in a ratio equal to 9:1 by constant stirring until spinning. The aligned cyanobacteria spun fibers were produced by oscillatory spinning at a rate of 260 opm and a constant pneumatic pressure of 0.7 bar extruded from a blunt needle 800 μm (21 G). The printhead moved along the Y-axis at a feed rate of 200 mm·min^{-1}.

3. Results and discussions

3.1. General description of the fiber formation

In this report, we introduce Fibroprinting—a novel approach that seamlessly integrates fiber spinning with 3D (bio)printing under a single setup, overcoming the limitations of existing fabrication methods and allowing additive manufacturing of fiber-reinforced composites. This method is based on a novel approach for biomimetic mechanical pulling of fibers from a polymer melt or solution—Oscillatory Fiber Spinning—and directly depositing them onto a 3D (bio) printing bed or platform, where another material can be printed interchangeably at a later time point. The method is inspired by the way spiders form silk fibers (Fig. 1**a**): a viscous protein solution ('silk dope') is extruded through spinnerets and mechanically drawn out into fine threads, where controlled pulling and shear forces align and solidify the material. The fibers are deposited in a stretched state that was confirmed by their ability to shrink upon heating and do not require additional support between the contact points, where they adhere to the 3D printing bed (object 1 in Fig. 1**b**). This enables the creation of long (ca. 10 nm) freestanding, non-sagging fibrous structures. To secure the fibers and prevent their contraction, adhesive layers are printed or applied at the points where the fiber ends meet the printing bed. To allow pulling of fibers, we use a rod (object 2 in Fig. 1**b**) fixed at both ends on an oscillating rod(s) (object 3 in Fig. 1**b**) to form an oscillating fiber spinning setup (Fig. 1**b**). In contrast to rotational (touch) spinning [20], where the rods are fixed at one end on a rotating disk, our setup performs a semicircular movement above a 3D printing bed (object 1 in Fig. 1**b**) back and forth (Movie S1, S2). Any setup allowing reciprocating movements can be used to achieve an oscillating movement [22].

This oscillating configuration offers several key advantages: (i) it enables the deposition of horizontal and long tilted freestanding fibers,

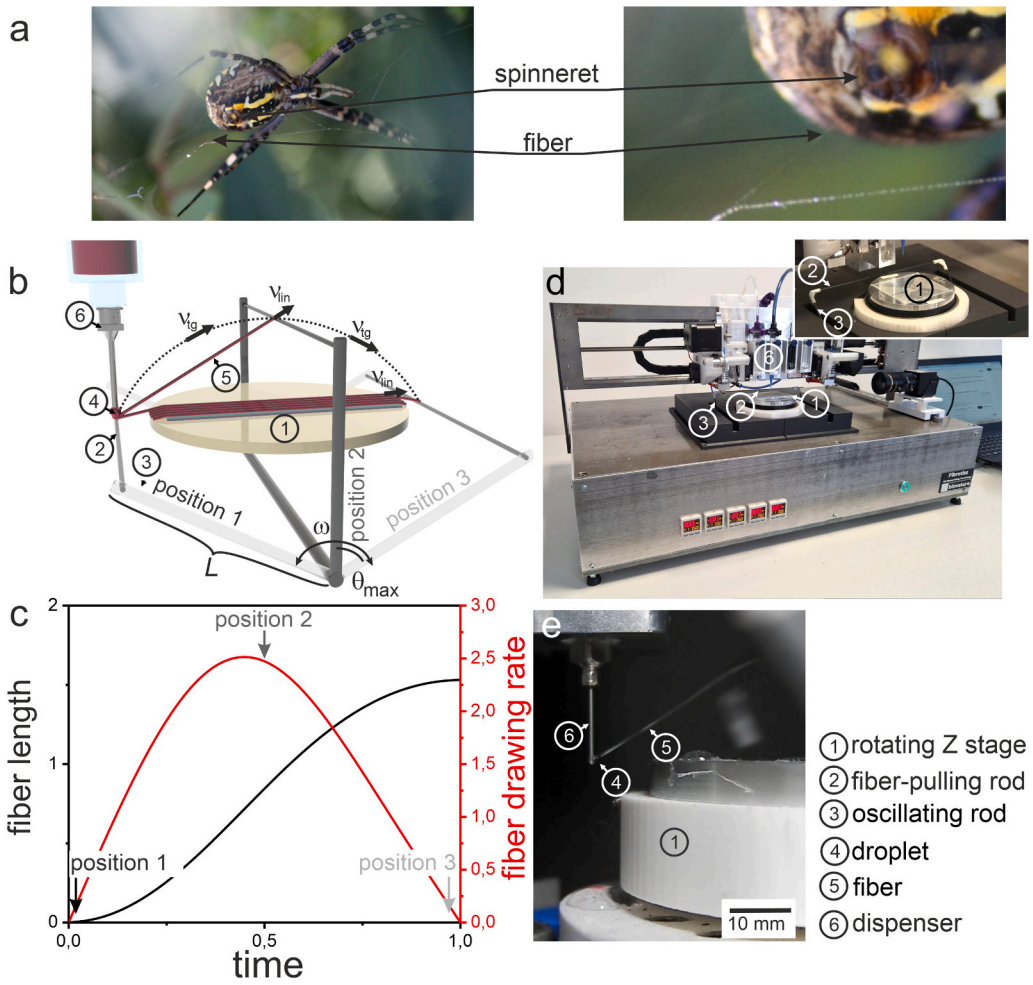


Fig. 1. Concept of mechanical fiber-spinning: (a) – mechanical fiber spinning in nature; (b) - schematic of fiber-spinning device unit integrated in (d, e) extrusion-based 3D printer, (c) - dependence of length of stretched fiber (black line) and linear rate of its stretching (red line lines).

which is not possible with electrospinning or melt electrowriting; (ii) the fiber pulling rate is precisely controlled and can vary from centimeters per second to several meters per second, which is not possible with electrospinning or melt electrowriting; (iii) unlike gravity spinning, the fibers are deposited on horizontal surface; (iv) the 3D printing bed, where fibers are deposited, and additional material is 3D printed, can move vertically without mechanical constraints allowing virtually any thickness of the sample, unlike in rotational (touch) spinning where rotation around samples restricts possible position of sample; (v) rotation of 3D printing bed allows deposition of fibers in different directions; and (vi) it is seamlessly compatible with extrusion-based 3D printing without introducing technical constraints, allowing using multiple extruders to be used interchangeably for both fiber spinning and 3D (bio) printing.

During each oscillation—from left to right and back over the printing stage—the fiber-pulling rod (object 2 in Fig. 1**b**) makes a contact with a droplet of polymer melt or solution (object 4 in Fig. 1**b**), draws a fiber (object 5, Fig. 1**b**), and deposits it onto the 3D printing bed (object 1 in Fig. 1**b,d,e**). The polymer solution or melt droplet can be generated using either a pneumatic-driven or filament-driven extruder. The motion of the oscillatory fiber-spinning setup can roughly be described as harmonic, similar to that of a pendulum. The angular position (Eq. 1) and corresponding distance ($X(t)$, Eq. 2) and movement rate of the fiber-pulling point relative to the droplet contact position ($\dot{X}(t)$, Eq. 3) are given by:

$$\theta(t) = \frac{\theta_{max}}{2}(1 - \cos(\omega t)) \quad (1)$$

$$X(t) = 2L\sin\left(\frac{\theta_{max}}{4}(1 - \cos(\omega t))\right) \quad (2)$$

$$\dot{X}(t) = \frac{L\theta_{max}\omega}{2}\sin(\omega t)\cos\left(\frac{\pi\theta_{max}}{4}(1 - \cos(\omega t))\right) \quad (3)$$

where θ_{max} is maximal deflection angle, ω is angular frequency, L is length of the rod (rod 3 in Fig. 1**b**). Eqs. (2) and (3) describe the fiber length $X(t)$ and drawing rate $\dot{X}(t)$ vs time, respectively. They show that under oscillatory motion, the stretching rate is zero at the moment of droplet contact, increases thereafter, and returns to zero as the fiber reaches the substrate (Fig. 1**b**, Figure S1a, Movie S1). Consequently, oscillatory spinning enables the rod to contact the droplet at very low speed, providing sufficient time for adhesion—governed by the relaxation time (λ) of the melt or solution. This feature makes oscillatory spinning particularly suitable for processing polymer melts or ultrahigh-molecular-weight polymer solutions, which exhibit high viscosity and long relaxation times. Such control is especially important, since polymer mechanical properties are strongly influenced by molecular weight through entanglement formation.

In contrast, during rotational (touch) spinning, the stretching rate is maximal at the point of droplet contact and gradually decreases as the rod approaches the substrate (Figure S1b). For electrospinning and melt electrowriting, describing and controlling stretching rates as time-

dependent functions is considerably more difficult; in practice, only average spinning rates are reported—ranging from a few centimetres per second to several meters per second in electrospinning, and from a few millimetres to several centimetres per second in melt electrowriting [4]. By comparison, our method provides precise control not only over the spinning rate: the technically achievable oscillating rate ranges from 70 oscillations per minute (opm) corresponding to average tangential speed $\overline{v_{tg}} = 0.36\ \mathrm{m{\cdot}s^{-1}}$ ($\overline{v_{tg}} = 2 \bullet$ number of full oscillations per second $\bullet$ length of arc) and average linear fiber spinning speed $\overline{v_{lin}} = 0.32\ \mathrm{m{\cdot}s^{-1}}$ ($\overline{v_{lin}} = 2 \bullet$ number of full oscillations per second $\bullet$ length of chord) to 850 opm, $\overline{v_{tg}} = 4.4\ \mathrm{m{\cdot}s^{-1}}$, $\overline{v_{lin}} = 3.9\ \mathrm{m{\cdot}s^{-1}}$ for 3D printer with integrated fiber-spinning unit illustrated in Fig. 1**d,** but also over its temporal profile during fiber formation, which is particularly advantageous for *in-situ* fiber spinning.

3.2. Effect of rheological properties on fiber formation

To prove the hypothesis that the character of fiber formation is determined by the rheological properties of spun materials, we investigated the effect of characteristic time (λ), which is *similar* to relaxation time, and zero shear viscosity (η_0) on fiber formation. For this, we used aqueous poly (ethylene oxide) (PEO) solutions with molecular weights ranging from 100 kDa to 8000 kDa across various concentrations. Water was used as the solvent to minimize the effects of evaporation and avoid concentration changes during the spinning process, allowing controlled model experiment; in a real experiment, the formed fiber must dry out during its formation. These PEO solutions exhibited classical rheological characteristics typical of polymer solutions or melts, dominated by weak intermolecular (van der Waals) interactions (Figure S2) - defined as zero shear viscosity and characteristic time. The fiber formation properties depend on the molecular weight and concentration of polymer (Figure S3). Viscosity as a function of shear rate followed a characteristic profile, which could be accurately modelled using the Cross equation, enabling the extraction of η_0 and λ values (Figure S4), which were fitted (Figure S4) using linear regression in log coordinates (Eqs. 4 and 5). We used the predicted values of η_0 and λ for further discussion, as these parameters could not always be reliably obtained from the Cross equation for all samples. In some cases, only the shear-thinning region of the rheological curve was measurable, whereas in others, only the zero-shear viscosity could be determined with confidence. Moreover, the use of fitted data helps to minimize errors arising from both measurement inaccuracies and imperfect fitting of the experimental results.

$$\log(\eta_0,\quad mPa \bullet s) = 3.5\log(Mw,\quad kDa) + 4.1\log\left(C,\quad g \bullet L^{-1}\right) - 13.3 \tag{4}$$

$$\log(\lambda,\quad s) = 3.44\log(Mw,\quad kDa) + 2.42\log\left(C,\quad g \bullet L^{-1}\right) - 15.03 \tag{5}$$

We mapped the fiber formation behavior (Figure S4) of these solutions as a function of characteristic time (λ) and zero-shear viscosity (η_0) obtained using equations above, as these two parameters govern the maximum achievable flow rate (Fig. 2**a1–2**). The same was also done for the cases when characteristic times were obtained using Cross fitting of rotational viscosity and Carreau fitting of complex viscosity without applying Eqs. (4) and (5) (Figure S5). In the viscous flow regime, the flow rate is primarily determined by η_0, whereas in the elastic regime—where the deformation rate exceeds the inverse of the characteristic time—the flow rate is controlled by λ. The map in the

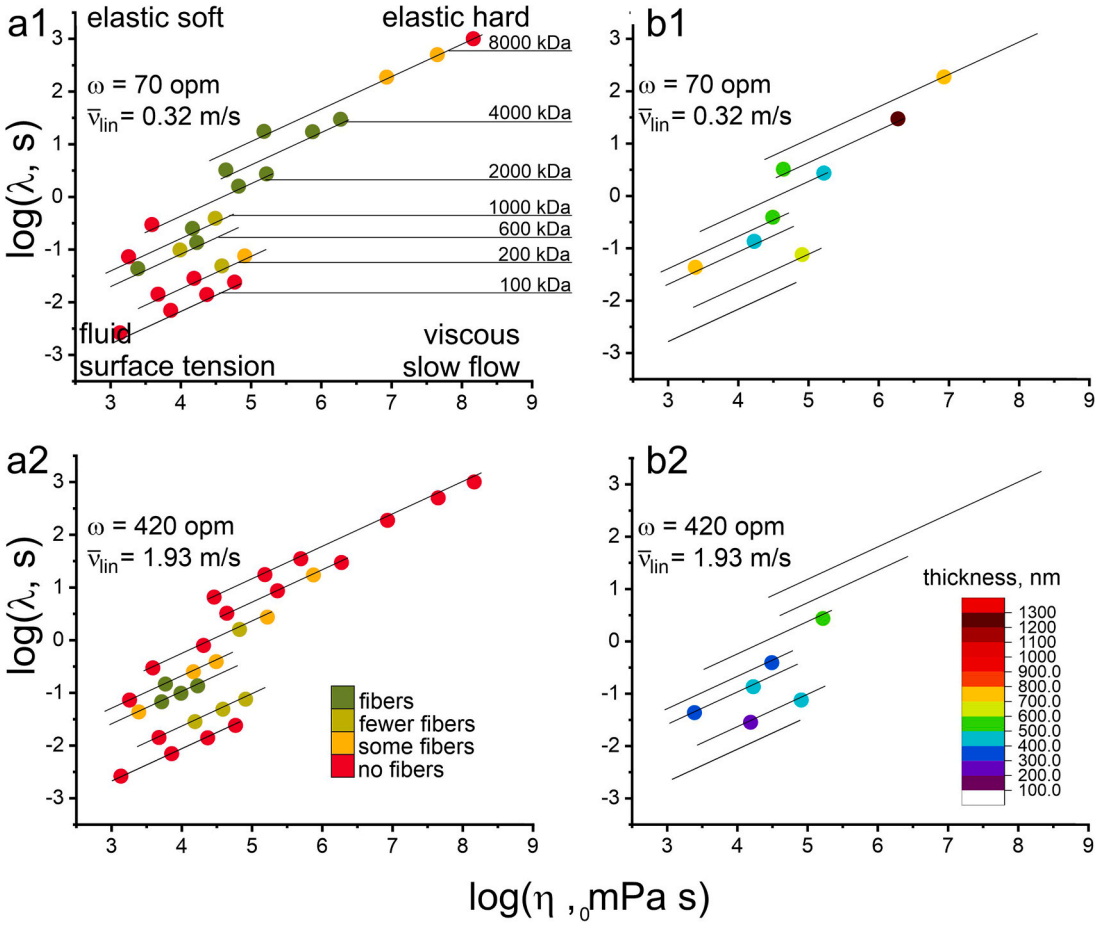


Fig. 2. Effect of rheological properties of PEO solutions on fiber formation: (a1-a2) maps of regimes of fiber formation and (b1-b2) dependence of fiber diameter on rheological properties (characteristic time λ and zero shear viscosity η_0 obtained using Cross fitting) of PEO water solutions.

coordinates λ, η_0 has 4 clear regimes: (i) low λ, low η_0—agile liquid, strong domination of surface tension; (ii) low λ, high η_0—viscous liquid, effect of surface tension is strong, but flow is retarded by high viscosity; (iii) high λ, low η_0—soft elastic material at fast deformation; (iv) high λ, high η_0—stiff elastic materials at fast deformation. Materials with a low relaxation time λ (flow-dominated regime) can be stretched almost indefinitely while their polymer chains remain largely relaxed. In contrast, materials with a high λ (elastic regime) behave like elastomers: they can typically be stretched by about 100%–1000%, depending on molecular weight, before failure occurs, during which their polymer chains become strongly stretched.

Our experiments reveal a defined window of λ and η_0 values within which stable fiber formation occurs (Movie S5-S7, Figure S6b**1–3**). At low λ and low η_0 (regime i), fibers do not form: surface tension forces break the filament during stretching, producing droplets on both the rod and the dispenser (Figure S6a**1–3**, Movie S4). In regime ii (low λ, high η_0), the contact of the rod to the material does not result in the formation of adhesive contact due to high viscosity and low contact time. In regime iii (high λ, low η_0), the rod establishes good adhesion with the extremely soft fiber-forming material, but the rapid motion leads to rupture (Figure S6e**1–3**, Movie S8). The maximal strain can be estimated as ~20 000–25 000% by considering a droplet size of 0.6 mm and a final fiber length of 15 cm—far exceeding the elastic limit of elastomeric materials. This indicates that a transition from viscous flow to elastic behavior must occur during fiber formation, driven by solvent evaporation, which in turn allows tailoring of polymer chain stretching. We observed that the soft elastic solution ($G_N \approx 45Pa$) got stretched to form a fiber (Figure S7, Movie S8), which ruptures at elongation ca. 3300% and returns to its initial drop-like shape that indicates a theoretical possibility to obtain highly stretched and oriented fibers. When both λ and η_0 are high, contact between the material and the rod cannot be established on a timescale of contact: the material simply rebounds upon impact (Figure S6f**1–3**, Movie S9). In this case, slower motion or longer dwelling time at the position of contact with the droplet would be required. Several transition regimes are also observed. For instance, fibers produced from materials with low η_0 and moderate λ tend to pull additional material from the droplet if it is large enough, since the stretched fibers contract upon relaxation (Figure S6c**1–3**, Figure 2**a1–3**). Fiber formation is dependent on oscillation frequency. Slower oscillations enable spinning of materials with high λ and η_0, as the longer contact time allows adhesion between the rod and the fiber-forming material. Another critical factor influencing this relationship is the material flow rate. At high oscillation frequencies, the outflow from the nozzle is reduced; if too little material is supplied, the resulting droplet is too small for the rod to make contact. Rotational (touch) spinning shows a similar character of window within which fibers are formed (Figure S8, Figure S5, Figure S9). Electrospinning shows more complex character of window within which fibers are formed, as it includes regime when multiple fibers (electrospinning) and singular fibers (electrowriting) are formed (Figure S5, S10). Generally, fibroprinting allows spinning of more viscous solutions than electrospinning – electrospinning of solutions of PEG $M_w = 8000$ kDa typically results in formation of thick fibers with beads, while fibroprinting forms straight bead-free fibers. Moreover, use of low-viscosity solutions for electrospinning results in formation of multiple fibers, while oscillatory spinning yields thin individual fibers when spinning is performed at high oscillation speed. Oscillational spinning and touch (rotational) spinning yield comparable results at the similar conditions ($\overline{v_{lin}} = 0.32\ m{\cdot}s^{-1}$ for oscillatory spinning and $\overline{v_{lin}} = 0.32\ m{\cdot}s^{-1}$ for rotational spinning in Figure S5)

We also demonstrated that fibers can be formed directly from polymer melts using filament extrusion (Figure S11). This extrusion approach offers several advantages: (i) high pressure can be applied to a portion of the molten filament, and (ii) only a small volume is heated, which minimizes polymer degradation. Two types of polymers were investigated — polyesters and polyurethanes. Polyesters show relatively simple rheological behavior, with a distinct zero-shear viscosity and characteristic time. They have only weak temperature dependence of viscosity and remain highly viscous even at elevated temperatures, which prevents proper contact between the rod and the droplet. In practice, melts with a suitable characteristic time are too viscous, while melts with acceptable viscosity have too short characteristic time. Such polymers can be spun from melt at relatively high temperatures around 400°C when zero shear viscosity is sufficiently low. Polyurethanes behave very differently because of strong hydrogen bonding. They show pronounced shear-thinning behavior and lack a measurable zero-shear viscosity in the temperature range where hydrogen bonds dominate. Their viscosity is strongly temperature-dependent: near the nozzle exit, the melt is fluid enough to establish proper contact with the rod, but cooling causes viscosity and characteristic time to increase sharply. This makes polyurethanes spinnable with our technique without the need for solvents or ultra-high-molecular-weight additives. A similar process occurs during solution spinning: the polymer solution, with its initially low viscosity, readily wets the rod but rapidly evaporates during fiber pulling, leading to a viscosity increase and a transition to the viscoelastic regime. Typically, polymer melts must be spun at high extrusion- and ambient temperatures to achieve sufficiently low zero-shear viscosity. This process differs markedly from spinning PEO from aqueous solution, as polymer melts cool down much faster than water evaporates from PEO solutions, leading to a rapid change in rheological properties during fiber drawing.

Polymers with low glass transition and crystallization temperatures—such as polyurethanes and high–molecular weight polycaprolactone (PCL80K) —tend to form straight fibers (Figure S11). Polymers with sufficiently low molecular weight (PCL45K) tend to form ruptured fibers as toughness needed for stretching scales with molecular weight – they are not tough enough to be strongly strecthed. In contrast, polymers with higher glass transition and crystallization temperatures, such as PLA and PA12, tend to produce wavy or wrinkled fibers. This behavior arises because fibers of high-T_g polymers solidify in air while still highly stretched and are deposited in an overstretched state that results in wavy structure. By contrast, polymers with low T_g retain elastomeric character during deposition and can relax or shrink if overstretched. Excessive stretching of already solidified polymers may even lead to rupture during spinning. We therefore hypothesize and preliminary experiments indicate that this hypothesis is correct that increasing the ambient temperature during melt spinning could delay solidification and enable higher-quality deposition of fibers from polymers with high glass transition and crystallization temperatures.

The fiber diameter is determined by a complex interplay between the material's rheological properties, which influence both the flow rate and the oscillation dynamics. The diameter of the dried fiber depends on the diameter of the spun, solvent-containing fiber and the polymer concentration in the solution. Increasing the polymer concentration generally leads to thicker dried fibers, as more solid material remains after solvent evaporation. However, higher concentration also reduces the flow rate, resulting in smaller droplets and, consequently, thinner fibers. This competition explains the absence of a clear correlation between fiber diameter and the rheological parameters λ and η_0 (Fig. 2**b1–2**). Indeed, we observed large fiber diameters for both highly viscous and weakly viscous solutions. For example, PEO (M_v ~ 8000 kDa, 20 $g{\cdot}L^{-1}$) fibers spun at low oscillation frequency (Movie S7) exhibited diameters of about 0.5 mm when droplets formed rapidly under high extrusion rates. Conversely, smaller fiber diameters were obtained at intermediate zero-shear viscosities and higher oscillation frequencies. Spinning from polymer melts generally produces relatively thick fibers (a few to several tens of micrometers) since the melt contains only polymer. In contrast, spinning from volatile polymer solutions enables the formation of much thinner fibers, particularly at low polymer concentrations. Here, we also spun polycaprolactone (PCL, M_n ~ 80 kDa) with a small addition of PEO 8 MDa from chloroform and nylon−6,6 from HFIP (0.14 $g{\cdot}L^{-1}$), obtaining fibers with diameters of ~0.2–1 μm and distinctive morphologies (Fig. 3). Two PCL-PEO fiber

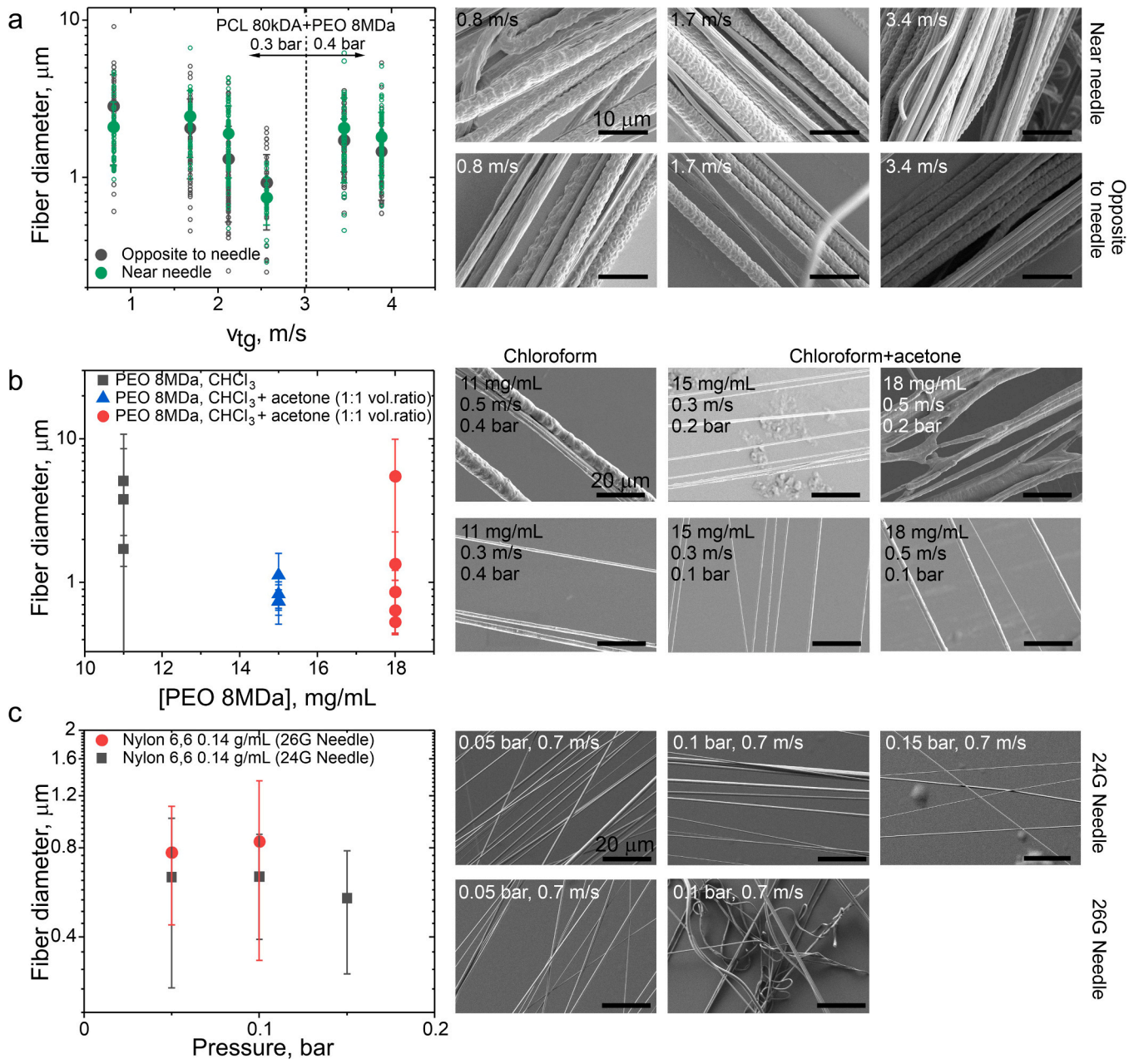


Fig. 3. Fibers formed by different polymers drawn from solutions: (a) 10 w/w% PCL (80 kDa) + 0.5 w/w% PEO in chloroform, PEO (8MDa) fibers in chloroform or chloroform-acetone mixture (b), Nylon 6,6 fibers in HFIP.

populations were observed: thicker fibers contained internal cavities, while in thinner fibers these cavities were highly elongated. We attribute this morphology to necking phenomena occurring during stretching above the polymer yield point, where elongated cavities represent a stage close to complete neck formation. Increase of spinning speed reduced fiber diameter (Fig. 3**a).** Increase of pressure applied to extrude polymer solution result in slight increase of fiber diameter (Fig. 3**a)**—the more material is extruded, and the thicker liquid fiber is drawn, the thicker will be dry fiber. Increase of concentration of the polymer is, as expected, results in formation of thicker fibers (Fig. 3**b).** Variation of needle diameter has a relatively small effect on fiber diameter (Fig. 3**c).** Overall, our method enables fabrication of fibers with diameters ranging from ~200 nm (Fig. 3)—comparable to those produced by electrospinning and rotational spinning—up to 1 mm (Figure S6d**1–3**).

3.3. *Controlled fiber deposition*

Fiber formation is strongly influenced by the size of the extruded droplet. Extrusion of very small droplets enables only minimal contact with the fiber-picking rod, resulting in the formation and deposition of uniform, ultra-thin fibers (Movie S1). In contrast, extrusion of larger droplets leads to the pickup of a greater volume of solution, promoting bead formation due to surface tension effects (Movie S3). These beads exhibit a higher moment of inertia, which delays their deceleration and deposition. As a result, they tend to travel farther from the intended deposition site, while air viscosity further reduces their settling rate.

The precision of fiber deposition depends on multiple factors. In particular, large droplets and very high oscillation speeds (Figure S12) reduce deposition accuracy. Large droplets lead to poorly defined contact with the fiber-pulling rod, while rapid motion amplifies the influence of air viscosity, slowing fiber settling and increasing the gap

between the fiber and the stage. Overall, the deposition precision follows an approximately Gaussian distribution, with a full width at half maximum (FWHM) of about 130 μm (length of fibers is ca. 5 cm, maximal distance from fiber to deposition stage is ca. 2 cm). Notably, the full width at half maximum (130 μm) is lower than inner needle diameter (250 μm). The fibers can be deposited on the top of any object with thickness. In order to demonstrate it, we deposited fibers on a finger (Figure S13) located between two rods covered by adhesive.

We demonstrated fabrication of different fiber patterns using oscillation spinning of poly [(R)−3-hydroxybutyric acid)] (P3HB) solution in chloroform (Fig. 4, Movie S10-S12). In order to ensure deposition of fibers in different directions, we used a rotating 3D printing bed or platform—fibers are always spun in one direction, but the different direction of their deposition was achieved by rotating the 3D printing bed. By using this setup, we produced structures where fibers are aligned uniaxially with homogenous density, uniaxially with different densities, bundled fibers, fibers crossed at 90° and 45°, crossed fibers deposited at different densities, crossed in the same and different Z planes, and radially oriented fibers (**Fig. 4a-l)**. To fix the fibers, we used adhesive tape attached to the 3D printing bed and 3D-printed polylactic acid (PLA) fiber fixing frame, which enabled secure fixation and easy removal of the sample from the printing bed for further investigations. As an indication that the fibers are stretched, we deposited straight fibers crossed at different *Z* planes. As one bundle of fibers was cut, they immediately contracted and wrapped around fibers of the second bundle (Fig. 4**k-n**). Very interesting results were obtained by using soft polycaprolactone (PCL, M_w ~ 50 kDa) frame, which was fabricated by melt electrowriting (Fig. 4**o,p**). After fabricating the lower part of PCL frame and spinning of P3HB, the ends of spun P3HB fiber were anchored with adhesive. The second part of the frame layer was then deposited on top, encapsulating the fibers. Fiber ends were mechanically cut, leaving the central portions suspended within the frame. Some contractions of fibers caused minor PCL frame deformation and buckling (Fig. 4**o,p**). A key advantage of PCL is its low crystallization temperature (30 – 35 °C): when deposited, it is still in a liquid state, allowing the second frame layer to adapt to the fibers and the first layer, ensuring robust fixation. This method thus enables the fabrication of frames with integrated aligned fibers, which can be later cut into small pieces and used, for example, for cell culture experiments (Fig. 4**q, r, and-s**). These examples clearly demonstrate the feasibility of fabricating diverse fiber patterns with our technique.

3.4. Combining 3D printing and fiber spinning

We demonstrated the integration of 3D (bio)printing with fiber spinning based on oscillatory motion to fabricate a variety of complex 3D structures. We printed a block of alginate blended with carboxymethyl cellulose (SCMC) biomaterial ink, and then spun a blend of PCL, (M_n ~ 80 kDa) with PEO (M_v ~ 8000 kDa) fibers across its surface (Fig. 5**a**). The fiber ends were anchored with polyborosiloxane adhesive (characterized by $G_N = 10^4$ Pa, $\lambda = 0.6$ s, $\eta_0 = 6000$ Pa·s), pre-deposited along the perimeter of the printing bed. The fibers remained straight, freestanding, and conformed to the block's shape, demonstrating that printed alginate SCMC structure can define both fiber geometry and

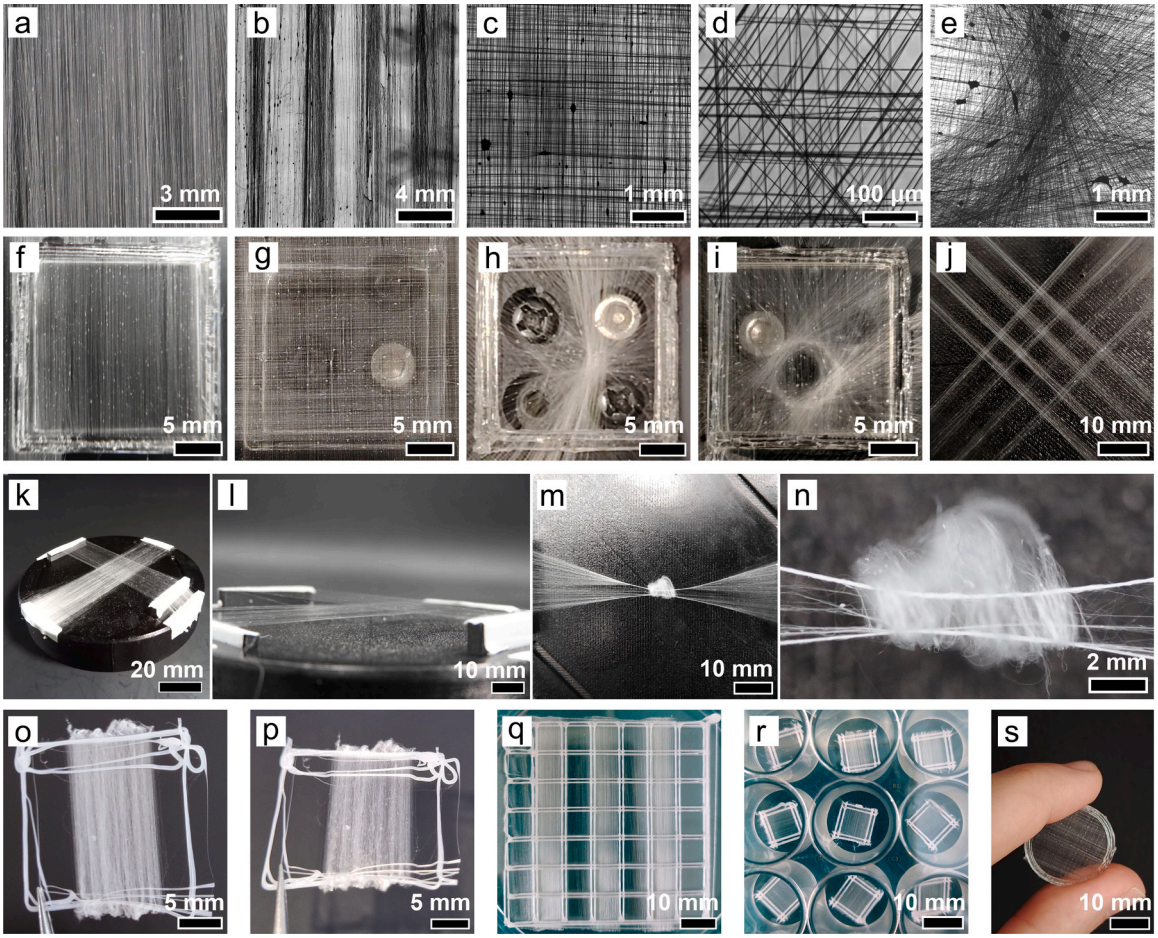


Fig. 4. Examples of fiber patterns obtained by oscillatory spinning include: (a,f) uniaxially aligned fibers; (b) uniaxially aligned fiber bundles; (c,d,g) crossed fiber networks; (e,h,i) radially arranged fibers; (j) crossed bundles of fibers; (k,l) fibers crossing at different z-planes; (m,n) structures shown in panels k and l after cutting one of the fiber bundles; (o,p,q,r,s) various samples deposited onto polymer frames.

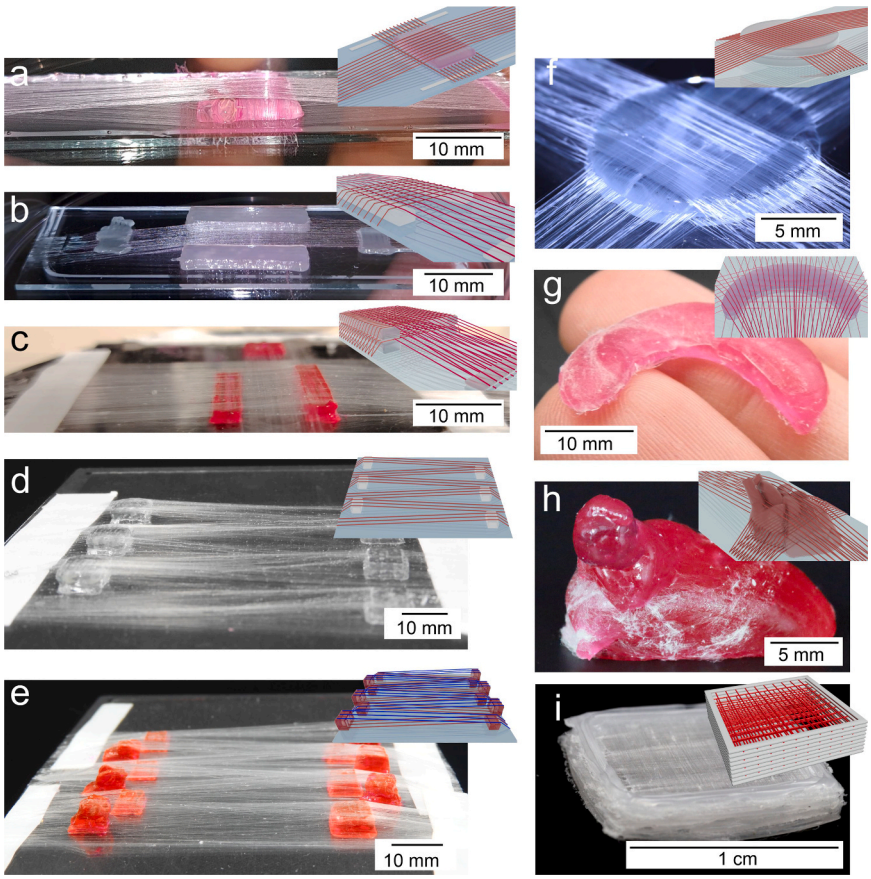


Fig. 5. Illustration of combination of 3D printing and oscillation fiber spinning, (a) – fibers deposited on the top of alginate SCMC block, (b,c) – crossed fibers supporting each other, (d,e) – tilted fibers that cross each other, (f) – several layers of fibers embedded in Laponite gel mimicking the structure of nucleus pulposus of intervertebral disk(g,h) – fiber reinforcement of self-healing gel in with the structure of knee meniscus (g) and the shape of heart (h). (i) – 3D fibrous structure formed by 40 alternating layers of fibers crossing each other at 90° and separated 3D printed frame. Gel materials are a) alginate SCMC, b) Vaseline, c-f) Laponite-RD, g and h) alginate with borax. Inserts show schematically location of fibers, different color of different fibers in (e) is for illustration purposes. More images are available in Fig. S14.

tilting angle.

In another experiment, we deposited intersecting long freestanding fibers that provided mutual structural support (Fig. 5**b**). An adhesive layer was again printed around the sample. Two tall parallel Vaseline (mixture of alkanes with plastic behaviour) blocks and two shorter perpendicular blocks were printed as supports. Polycaprolactone (PCL)–poly(ethylene oxide) (PEO) fibers were first spun between the tall blocks. After rotating the sample 90°, a second fiber layer was spun between the shorter blocks, crossing above the first. The central portion of the second layer was suspended, stabilized by the first-layer fibers. This yielded a 3D framework where orthogonal fiber layers reinforced one another, showing that deposition can occur at inclined angles rather than being limited to orientations parallel to the printing stage. Building on this experiment, we produced a similar, but two-layer structure composed of duplicated elements, which yielded two parallel layers of crossed long freestanding fibers (Fig. 5**c**).

One of the main advantages of our technique is its ability to deposit long freestanding, tilted fibers. Such fibers, as we anticipate, hold strong potential for interlayer reinforcement. To demonstrate this capability, we performed two experiments exploring diverse configurations for tilted fiber deposition. In the first experiment, two parallel rows of Laponite-RD hydrogel bricks, which exhibit pseudoplastic behavior (flow above a threshold stress), were printed in a chessboard pattern, where each brick was positioned opposite an empty space in the adjacent row. Fiber spinning on this structure produced alternating arrays of fibers tilted either left-to-right or right-to-left (Fig. 5**d**). In the second experiment, we fabricated two layers of vertically intersecting fibers by sequentially printing bricks of different heights arranged in a checker-like pattern (Fig. 5**e**). In both experiments, vertically crossed and tilted fibers may enable interlayer reinforcement when the surrounding space is filled with 3D-printed material.

In the next experiments, we created sandwich-like structures by embedding fibers within printed gel layers and created fiber-reinforced gel composites (Fig. 5**f**). A Laponite-RD layer in the shape of *nucleus pulposus* of the intervertebral disk was printed, followed by fiber deposition, and the process was repeated. Each successive gel layer induced the underlying fibers to adhere due to their flexibility and capillary forces, which deformed and pulled fibers into contact. In another variant of the gel reinforcement experiment (Fig. 5**g**,**h**), we used alginate–borax viscoelastic solutions with a relaxation time of approximately $\lambda \approx 10$ s and a plateau modulus of $G_n \approx 1$ kPa. This material behaves as a soft elastic gel on timescales shorter than the relaxation time, while it flows on longer timescales—exhibiting the typical "self-healing" behavior. Reinforcing this 3D printed gel in the shape of a knee meniscus with a network of crossed internal fibers and randomly oriented surface fibers led to a pronounced change in its relaxation behavior. The elastic fibers effectively restrict large-timescale spreading, which is otherwise observed in the pure, fiber-free gel. We also demonstrated printing of even more complex 3D geometries and their reinforcement with fibers. For this, we printed an alginate–borax viscoelastic solution in the shape of a heart's cross-section and reinforced it with crossed and radial fibers. Similar to the previous experiment, the fibers prevented the spreading of the 3D-printed self-healing gel under its own weight. These preliminary findings demonstrate that fibers substantially influence the viscoelastic

behavior of gel composites.

We demonstrated the fabrication of multilayer 3D fibrous structures (Fig. 5**i**). Specifically, 8 alternating layers of fibers, crossing each other at 90° and supported by a 3D-printed frame, were constructed. The fibers were anchored to the frame yet remained free-standing between the frame elements, with a spacing of 1 cm. These experiments highlight the unique capability of combining 3D printing with in-situ mechanical spinning, enabling structures that cannot be achieved using conventional methods.

3.5. Mechanical properties

We next developed a dedicated approach to measure the mechanical properties of fibers. This task is highly challenging because the fibers are extremely thin and flexible, which complicates their handling and reliable fixation in a tensile testing machine. To overcome this limitation, we designed a custom-made 3D printed sample holder consisting of a rigid frame with two adhesive bands to which the fibers were glued, incorporating narrow neck regions (Fig. 6**a1**). After mounting the frame in the tensile tester, the narrow necks were cut, thereby releasing the fibers while maintaining secure fixation at both ends (Fig. 6**a2**). This procedure enabled stable uniaxial stretching of the fibers and reliable measurement of their mechanical properties (Fig. 6**a3,4**).

The fibers exhibited a pronounced reinforcing effect (Fig. 6**b,c**). To demonstrate this at the construct level, we fabricated a 3D-printed PCL frame containing three layers of P3HB fibers, with uncrosslinked alginate solution prepared in cell culture medium printed between each fiber layer – a prototype of fiber-reinforced visco-elastic gel. In the absence of Ca^{2+} crosslinking, alginate behaves as a viscous liquid with no intrinsic mechanical stability and cannot be handled manually (Movie S15). However, incorporation of the fibrous mesh transformed the material into a gel-like construct that could be easily manipulated, as the fibers effectively reinforced the soft matrix (Fig. 6**b,c,** Movie S16). Tensile testing of these constructs was subsequently performed (Fig. 6**c3**), revealing that the fibrous network functions analogously to a sponge, providing mechanical integrity to an otherwise fluid matrix. Notably, the deformation behavior of the fibrous mesh differs fundamentally from that of bulk polymers: individual fibers can irreversibly rearrange relative to one another under load, leading to pronounced loading–unloading hysteresis. Such materials are particularly attractive for tissue engineering applications, as they combine high porosity with mechanical stability while containing a large fraction of low-viscosity fluid (the fiber mass fraction is below 1%), which is essential for cell mobility.

We also demonstrated reinforcement of elastomers (Fig. 6**d1,d2)**. For this purpose, fiber-reinforced silicone structures were fabricated by 3D printing a cream-like material into a frame geometry with multiple embedded fiber layers (Figure S15). The 3D printed structure was subsequently filled with a two-component silicone mixture and allowed to cure. Mechanical properties were evaluated using indentation testing, with fibers aligned parallel to the horizontal direction. Both samples exhibit a J-shaped stress–strain response. However, the fiber-reinforced silicone shows a higher initial modulus at low strains and an earlier transition to a steep stress increase, which can be attributed to the reinforcing effect of the embedded fibers.

We further demonstrated the reinforcing effect of the spun fibers in an inorganic particulate material, using gypsum as a model system. In this experiment, a fiber layer was first deposited with the fiber-spinning unit of our device. Subsequently, a small amount of gypsum powder was manually distributed onto the fiber mat, followed by the addition of several drops of water to initiate hydration and setting. Although the manual powder deposition and the very fine particle size of the gypsum resulted in a non-uniform layer with suboptimal quality, the setup was sufficient to validate the feasibility of the approach. Importantly, the experiment clearly demonstrated effective reinforcement of hydrated gypsum by the embedded fibers. After crack formation, the structural integrity of the sample was maintained, as the fibers acted as crack-bridging elements, preventing catastrophic failure and preserving cohesion of the fractured parts (Figure S16).

3.6. Cell culture experiments

Fibroprinting allows fabrication of substrates for 2D and 3D cell culture. As examples, we prepared constructs with bundled (Fig. 7**a1**), crossed at different angles (Fig. 7**a2**), uniaxially aligned, and radially arranged (Fig. 7**b**) freestanding fibers using spinning from solvent. For these particular experiment the samples were dried at room temperature overnight, the amount of residual solvent was not assessed. For the radially arranged sample, the nozzle was positioned off-center relative to the rotation axis of the printing bed, creating a fiber-free central zone. As a result, the construct exhibited two distinct radial gradients: (i) fiber density and (ii) the angle between neighboring fibers. The thickness was likely non-uniform—greatest in fiber-dense regions and gradually decreasing toward the periphery. In these dense zones, cell visualization was challenging due to high cell and fiber densities. To enable imaging, we focused instead on the central region, which had comparable thickness but lower fiber density, resulting in greater transparency (Fig. 7**c1-c3**). In this area, we successfully visualized mouse fibroblasts (BALB 3T3) filamentous actin (F-actin) and nuclei across different Z-planes (Fig. 7**c1-c3**). These experiments clearly demonstrate the potential of our method for fabricating 3D complex structures in cell culture. We also demonstrated that cells are able to follow the pattern of produced fibers: cells are randomly oriented on random fibers (Fig. 7**d1**), uniaxially oriented on aligned fibers (Fig. 7**d2),** and follow the direction of either vertical or horizontal fibers when they are crossed **(**Fig. 7**d3).** We have also tested more complex cell viability in gel-fiber constructs, where 3D bioprinting of the bioink and preparation of the sample took a longer time (0.5–1 h). In one experiment, human cardiomyocytes differentiated from induced pluripotent stem cells (iPSCs) were bioprinted using alginate-SCMC bioink, with P3HB fibers deposited between each bioink layer. The cells remained viable and were able to migrate within the gel and anchor to the fibers. **(**Fig. 7**e).** In another experiment, Adult Normal Human Dermal Fibroblasts (NHDF) were seeded on top of freestanding bundled P3HB fibers and transforming growth factor-beta 1 (TGF-β 1) was added *promoting* collagen type I deposition. As a control, growth medium without growth factor was added to NHDF cells, showing normal collagen type I deposition (Figure S17). In another experiment, NHDF cells were seeded on aligned P3HB freestanding fibers and directly monitored cell motility using live cell microscopy for 24 h under physiological conditions. Cells were able to adhere and align to the fibers and move along the fiber's length in 2D (Movie S13) and 3D view (Movie S14). We believe that stabilizing non-crosslinked gels (polymer solutions) with reinforcing fibers, rather than by conventional crosslinking, will promote higher cell motility within the fabricated 3D constructs and thereby accelerate tissue formation and maturation.

3.7. Encapsulation inside fibers

Finally, we demonstrated the feasibility of encapsulating objects within the spun fibers. As a representative example, we encapsulated living organisms—cyanobacteria (Fig. 8). For this proof-of-concept study, rod-shaped cyanobacteria were incorporated into an aqueous PEO solution (Mv ≈ 2000 kDa, 40 $g{\cdot}L^{-1}$) at a volume ratio of 1:9 (cyanobacteria:PEO), which was subsequently used for fiber fabrication. The spinning rate and PEO concentration were adjusted to produce relatively thick fibers, comparable to those shown in Figure S6d**1–d3**. Under these conditions, the fibers dried gradually and were deposited in a liquid-like state, enabling the formation of patterned structures containing aligned, elongated cyanobacterial filaments. More broadly, this strategy can be readily extended to the encapsulation of a wide range of functional payloads, including liquid droplets, solid particles, and other dispersed

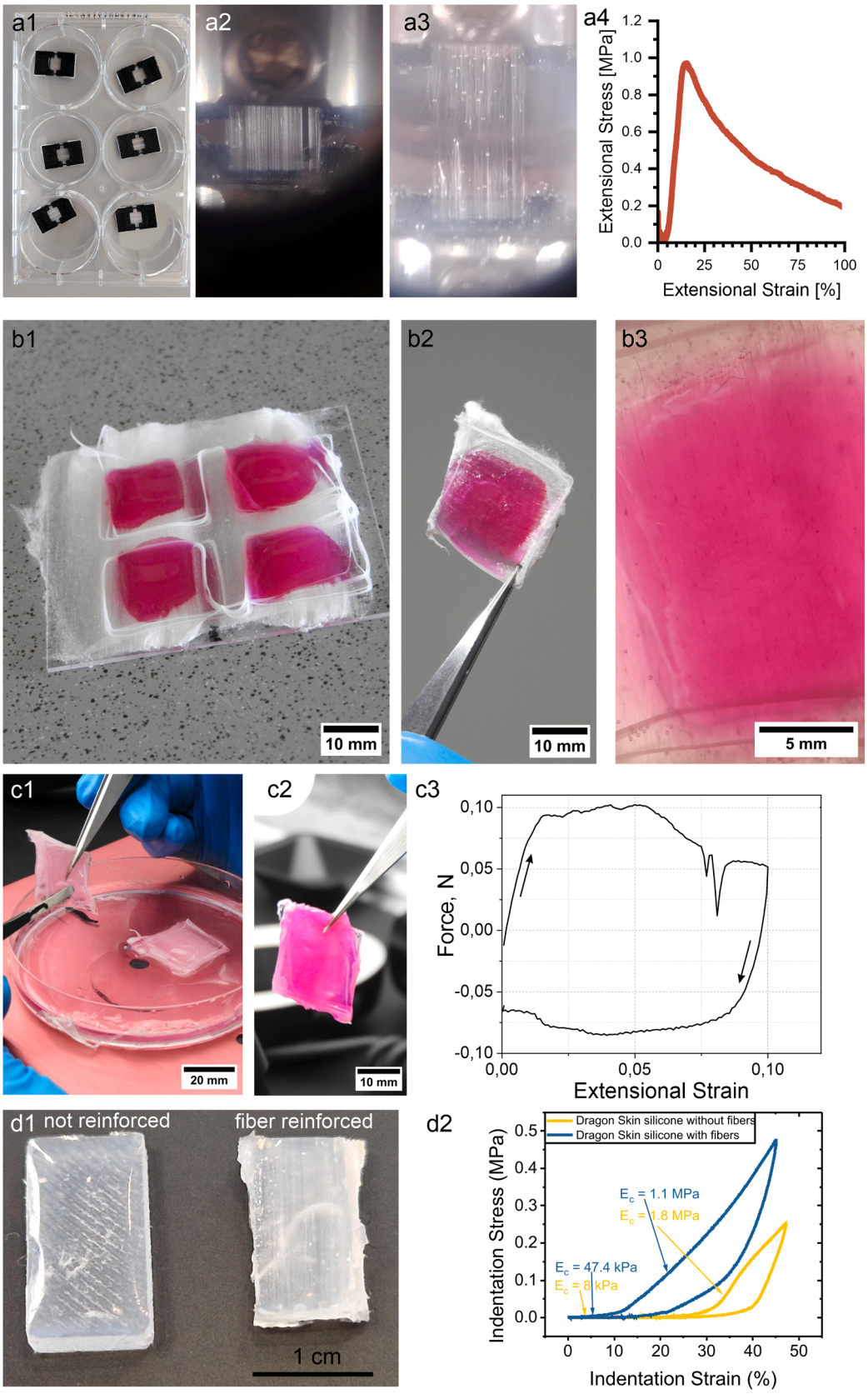


Fig. 6. Illustration of the fiber-reinforcement effect of fibers. (a1-a3) images of P3HB fibrous as prepared sample (a1), during testing (immersed in buffer saline PBS) (a2) after failure (a3) and final stress- strain dependence (a4); (b1-b3) uncrosslinked alginate solution reinforces with P3HB fibers; (c1-c3) fiber-reinforced alginate samples can be manually handled and their mechanical properties measured, which is not possible with non-reinforced alginate solution; (d1-d2) not reinforced and fiber reinforced silicone as well as their indentation test.

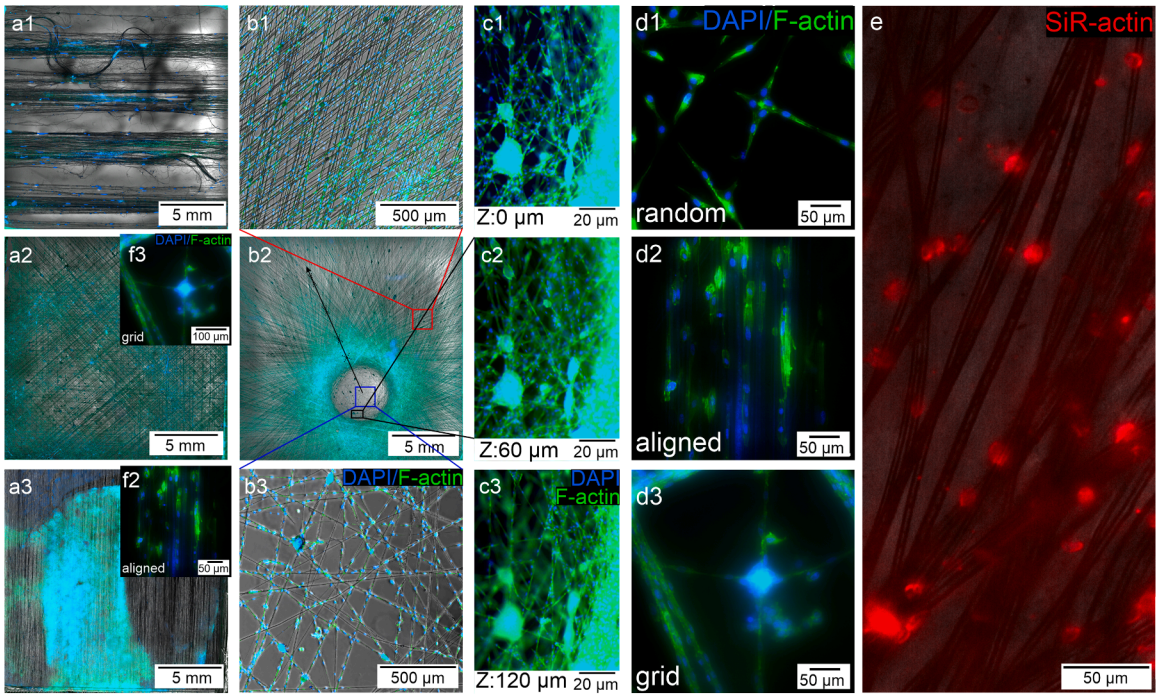


Fig. 7. 3D cell culture in fibrous layers: (a1-a3) Large-scale images of fibrous samples with cultured cells, showing inhomogeneous cell seeding caused by rapid sedimentation; (b1-b3) Large-scale image and magnified views of two regions of a sample with cells cultured on radially deposited fibers; (c1-c3) DAPI, FITC, and merged DAPI–FITC fluorescence images of cells on radially deposited fibers acquired at different relative z-planes (0, 60 and 120 µm); (d1-d3) Cell alignment and attachment on random, aligned and crossed fibers in higher magnification (40x), (e) P3HB fiber–reinforced AA-SCMC (embedded iPSC-cardiomyocytes) bioink.

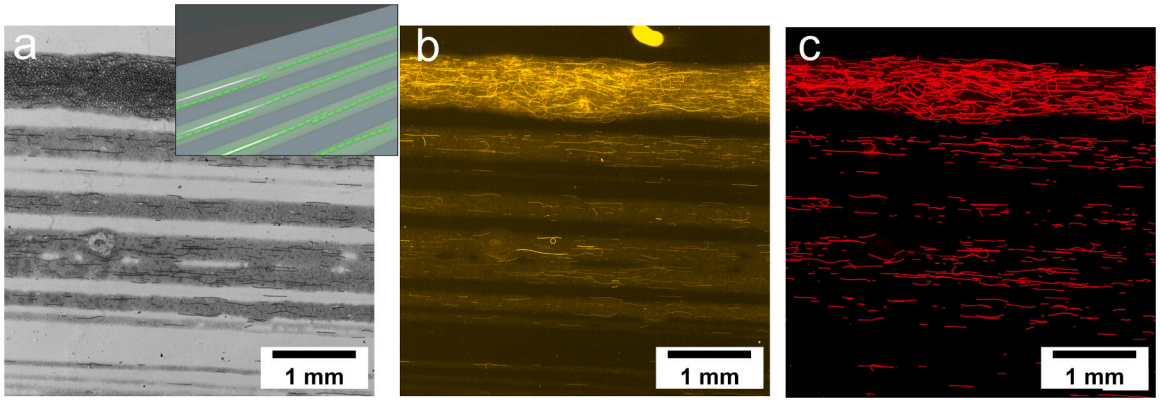


Fig. 8. Illustration of fiber spinning with embedded living organisms (cyanobacteria *Lyngbya lagerheimii*), a,b,c- imaging using different wavelength filter.

phases, highlighting the versatility of the spinning approach.

3.8. Comparison of fibroprinting with melt electrowriting and electrospinning

At the end, we compared fibroprinting with electrospinning and melt-electrowriting (Table 1). Fibroprinting exhibits lower spatial precision in fiber deposition, primarily due to the relatively large initial distance between the forming fiber and the substrate. While higher precision can be achieved with melt-electrowriting, this advantage is not critical for most practical applications, such as material reinforcement or scaffold fabrication. In contrast, fibroprinting provides capabilities that are not accessible with electrospinning or electrowriting. Finally, we analyzed the rheological regimes governing each technique (Fig. 9). Electrospinning operates in both viscoelastic and viscous regimes, electrowriting is confined to the viscous regime, and fibroprinting operates in the viscoelastic regime. These distinctions indicate that the methods are complementary rather than mutually exclusive. Their combination can be leveraged to exploit their respective advantages while mitigating inherent limitations that is why the machine shown in Fig. 1d is equipped with possibilities to connect high-voltage power supply to allow combination of fibroprinting, electrospinning and electrowriting.

4. Conclusions

In this work, we introduce—for the first time—a powerful true integration of high-speed *in situ* biomimetic mechanical fiber spinning with 3D (bio) printing through an oscillatory fiber-spinning unit. This approach brings together advantages that no currently existing fiber-spinning method can offer: (i) deposition of horizontal and tilted free-standing fibers, beyond the reach of electrospinning or melt electrowriting; (ii) precise and wide-range control over fiber pulling rates, from just a few centimeters per second to several meters per second—orders

Table 1
Comparison of fibroprinting, electrospinning and electrowriting.

Qualities	Fibroprinting	Electrospinning	Electrowriting
Free-standing fibers	very long, ca. 10 nm at least	short	short, ca. 1 mm
Programmed deposition	yes, with limited precision	very limited	yes, with limitations
Sample thickness	unlimited	few mm	10 mm
Fiber thickness	from 100 nm	from 10 nm	from 800 nm, typically 10 µm
Interlayer reinforcement	possible	limited	limited
Fiber deposition rate	up to several m/s	up to several m/s	several cm/s
Stretched fibers	yes	yes	no
Integration in 3D printing	yes	limited	yes
Polymer type	solutions and melts	solutions	melts
Voltage needed	-	8–40 kV	1–15 kV

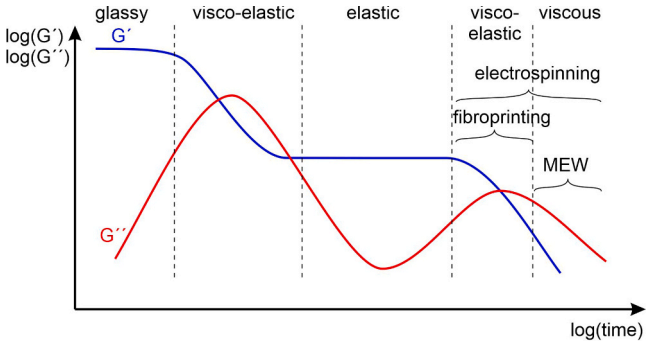


Fig. 9. Regimes of deposition of fibers in fibroprinting, electrospinning and electrowriting.

of magnitude broader than conventional techniques; (iii) unrestricted vertical motion of the 3D printing bed, enabling the creation of structures with virtually unlimited thickness, unlike in rotational (touch) spinning; (iv) programmable 3D printing bed rotation for controlled fiber alignment in diverse orientations; and (v) seamless compatibility with extrusion-based 3D printing, achieved without imposing technical constraints. Together, these features establish a versatile platform with exceptional potential. The method paves the way for a wide range of applications based on fiber-reinforced composited fabricated by additive manufacturing, from the fabrication of architected 3D scaffolds for tissue engineering to the encapsulation of living and non-living materials within fibers, structural reinforcement of composites, and the design of entirely new classes of functional materials.

CRediT authorship contribution statement

Olga Rusu: Investigation. **Ilia Sadilov:** Investigation. **Pavel Milkin:** Investigation. **Janina Rebhan:** Investigation. **Selma Padilla Padilla:** Investigation. **Ceyda Topal:** Investigation. **Md Fakrul Bin Kabir:** Investigation. **Alla Synytska:** Investigation. **Waseem Kitana:** Investigation. **Zhander Vohr Soreño:** Investigation. **Leonid Ionov:** Writing – review & editing, Writing – original draft, Conceptualization. **Gissela Constante:** Investigation. **Indra Apsite:** Investigation.

Funding

Authors acknowledge DFG IO 68 14–1 (AOBJ: 656679), DFG IO 68 14–2 (AOBJ: 710120, Project number 409232653), 326998133 – TRR 225 (subprojects A08, B11), Joachim Herz Foundation for financial support.

Declaration of Competing Interest

The authors declare the following financial interests/personal relationships which may be considered as potential competing interests: Leonid Ionov and Alla Synytska are beneficiaries and owners of biovature GmbH, which holds a patent on the fiber spinning unit used in the combined 3D printer–fiber spinner described in this work. The other authors declare no competing interests. AI was used for proof reading of manuscript and language correction.

Acknowledgement

Authors acknowledge Thorsten Pretsch and Denis Schönfeld for providing of polyurethanes.

Appendix A. Supporting information

Supplementary data associated with this article can be found in the online version at doi:10.1016/j.addma.2026.105262.

Data availability

Data will be made available on request.

References

[1] A. Cano-Vicent, M.M. Tambuwala, S.S. Hassan, D. Barh, A.A.A. Aljabali, M. Birkett, A. Arjunan, Á. Serrano-Aroca, Fused deposition modelling: current status, methodology, applications and future prospects, Addit. Manuf. 47 (2021) 102378.
[2] E.M. Sefene, State-of-the-art of selective laser melting process: a comprehensive review, J. Manuf. Syst. 63 (2022) 250–274.
[3] B. De, M. Bera, D. Bhattacharjee, B.C. Ray, S. Mukherjee, A comprehensive review on fiber-reinforced polymer composites: Raw materials to applications, recycling, and waste management, Progress. Mater. Sci. 146 (2024) 101326.
[4] W. Kitana, I. Apsite, L. Ionov, 3D (Bio) Printing combined fiber fabrication methods for tissue engineering applications: possibilities and limitations, Adv. Funct. Mater. (2025) 2500450 (n/a (n/a)).
[5] S. Carosella, S. Hügle, F. Helber, P. Middendorf, A short review on recent advances in automated fiber placement and filament winding technologies, Composites Part B Engineering 287 (2024) 111843.
[6] A. Brasington, C. Sacco, J. Halbritter, R. Wehbe, R. Harik, Automated fiber placement: A review of history, current technologies, and future paths forward, Compos. Part. C Open. Access. 6 (2021) 100182.
[7] P. Cheng, Y. Peng, S. Li, Y. Rao, A. Le Duigou, K. Wang, S. Ahzi, 3D printed continuous fiber reinforced composite lightweight structures: A review and outlook, Composites Part B Engineering 250 (2023) 110450.
[8] J. Xue, T. Wu, Y. Dai, Y. Xia, Electrospinning and electrospun nanofibers: methods, materials, and applications, Chem. Rev. 119 (8) (2019) 5298–5415.
[9] P.G. Saiz, A. Reizabal, J.L. Vilas-Vilela, P.D. Dalton, S. Lanceros-Mendez, Materials and strategies to enhance melt electrowriting potential, Adv. Mater. 36 (24) (2024) 2312084.
[10] A. Hrynevich, P. Achenbach, T. Jungst, G.A. Brook, P.D. Dalton, Design of suspended melt electrowritten fiber arrays for Schwann cell migration and neurite outgrowth, Macromol. Biosci. 21 (7) (2021) 2000439.
[11] D. Jao, V.Z. Beachley, Continuous dual-track fabrication of polymer micro-/nanofibers based on direct drawing, ACS Macro Lett. 8 (5) (2019) 588–595.
[12] L.F. Deravi, N.R. Sinatra, C.O. Chantre, A.P. Nesmith, H. Yuan, S.K. Deravi, J. A. Goss, L.A. MacQueen, M.R. Badrossamy, G.M. Gonzalez, M.D. Phillips, K. K. Parker, Design and fabrication of fibrous nanomaterials using pull spinning, Macromol. Mater. Eng. 302 (3) (2017) 1600404.
[13] Li, Z.; Cui, Z.; Zhao, L.; Hussain, N.; Zhao, Y.; Yang, C.; Jiang, X.; Li, L.; Song, J.; Zhang, B.; Cheng, Z.; Wu, H., High-throughput production of kilogram-scale nanofibers by Kármán vortex solution blow spinning. Science Advances *8* (11), eabn3690.
[14] N.S. Yadavalli, D. Asheghali, A. Tokarev, W. Zhang, J. Xie, S. Minko, Gravity Drawing of Micro- and Nanofibers for Additive Manufacturing of Well-Organized 3D-Nanostructured Scaffolds, Small 16 (11) (2020) 1907422.
[15] M.R. Williamson, A.G.A. Coombes, Gravity spinning of polycaprolactone fibres for applications in tissue engineering, Biomaterials 25 (3) (2004) 459–465.
[16] Z. Ni, Z. Zhu, Y. Ji, X. He, X. Fu, W. Yang, Y. Wang, Biomimetic microadhesion guided instant spinning, Nano Lett. 22 (23) (2022) 9396–9404.
[17] S. Gantenbein, C. Mascolo, C. Houriet, R. Zboray, A. Neels, K. Masania, A. R. Studart, Spin-printing of liquid crystal polymer into recyclable and strong all-fiber materials, Adv. Funct. Mater. 31 (52) (2021) 2104574.
[18] X. Bai, S. Liao, Y. Huang, J. Song, Z. Liu, M. Fang, C. Xu, Y. Cui, H. Wu, Continuous draw spinning of extra-long silver submicron fibers with micrometer patterning capability, Nano Lett. 17 (3) (2017) 1883–1891.

[19] D. Jao, X. Hu, V. Beachley, Bioinspired Silk Fiber Spinning System via Automated Track-Drawing, ACS Appl. Bio Mater. 4 (12) (2021) 8192–8204.
[20] A. Tokarev, D. Asheghali, I.M. Griffiths, O. Trotsenko, A. Gruzd, X. Lin, H.A. Stone, S. Minko, Touch- and brush-spinning of nanofibers, Adv. Mater. 27 (41) (2015) 6526–6532.
[21] W. Kitana, V. Levario-Diaz, E.A. Cavalcanti-Adam, L. Ionov, Biofabrication of Composite Bioink-Nanofiber Constructs: Effect of Rheological Properties of Bioinks on 3D (Bio)Printing and Cells Interaction with Aligned Touch Spun Nanofibers, Adv. Healthcare Mater. 13 (2024) 2303343, https://doi.org/10.1002/adhm.202303343.
[22] Ionov, L.; Synytska, A. Device for fabrication of fibers, 3D printer comprising the device and method for fabrication of fibers. EP 22 208 882.5, 2022.